Analysis of the elastic properties of an interpenetrating AlSi12–Al2O3 composite using ultrasound phase spectroscopy

Siddhartha Roy, Oliver Stoll, Kay A. Weidenmann, Alwin Nagel, Alexander Wanner

Angaben zur Veröffentlichung / Publication details:

Roy, Siddhartha, Oliver Stoll, Kay A. Weidenmann, Alwin Nagel, and Alexander Wanner. 2011. "Analysis of the elastic properties of an interpenetrating AlSi12–Al2O3 composite using ultrasound phase spectroscopy." *Composites Science and Technology* 71 (7): 962–68. https://doi.org/10.1016/j.compscitech.2011.02.014.

Analysis of the elastic properties of an interpenetrating AlSi12–Al_2O_3 composite using ultrasound phase spectroscopy

Siddhartha Roy [a,*], Oliver Stoll [a], Kay André Weidenmann [a], Alwin Nagel [b], Alexander Wanner [a]

[a] Institut für Angewandte Materialien, Karlsruher Institut für Technologie, Kaiserstr. 12, D-76131 Karlsruhe, Germany
[b] Hochschule Aalen, Beethovenstr. 1, 73430 Aalen, Germany

1. Introduction

Metal–matrix composites (MMCs) typically exhibit enhanced specific mechanical properties in comparison to monolithic metals of which they are made [1]. MMCs can be classified according to the form of the reinforcement (such as fibres, particles, whiskers or short fibres, interpenetrating etc). Among these, MMCs having an interpenetrating structure have been shown to possess better strength, toughness and wear resistance in comparison to other composite structures [2,3]. Hence, much recent work has focussed on the development and analysis of interpenetrating metal–matrix composites. These include MMCs fabricated by reaction synthesis [4–6], by melt infiltration in wood ceramics [7], in 3-D periodic preforms produced by robotic deposition [8], in porous ceramic preforms fabricated by freeze-casting [9,10].

Recently, several studies have been carried out to analyse the elastic properties of composites having an interpenetrating structure [11–13]. Young's modulus and/or shear modulus of the composites were determined and the results were compared with numerous micromechanical models such as Hashin–Shtrikman (HS) bounds [14], Ravichandran (R) model [15], Tuchniskii (T) model [16] and effective medium approximation (EMA) [13].

The purpose of the present study is to carry out in depth analysis of the elastic properties of an interpenetrating AlSi12–Al_2O_3 composite. The composites were fabricated by direct squeeze-casting a eutectic aluminium–silicon (AlSi12) melt in an open porous alumina preform. The preform was fabricated by pyrolysis of cellulose fibres used as pore forming agent, pressing of the green ceramic body and subsequent sintering of alumina particles. Previous studies [11–13] on the elastic properties of interpenetrating metal/ceramic composites considered the composite to be isotropic. In the current study, the three longitudinal and the three shear elastic constants of composites with alumina contents varying in the range of 18–65 vol.% will be studied using ultrasound phase spectroscopy (UPS) [17]. As longitudinal and shear elastic constants are determined along all three directions, the extent of anisotropy can be investigated. The results are compared with several micromechanical models (HS-model, R-model, Feng (F) model, self consistent (SC) method and differential effective medium (DEM) approximation). These analyses show that the studied composites are not isotropic. Hence, assuming orthotropic symmetry, all nine elastic constants of the stiffness matrix of one sample will be determined. In a previous study, we investigated the mechanism of internal load transfer in this material under compression and tension [18]. The current study, along with this previous one helps to thoroughly understand the mechanics of this complex composite structure.

---

[*] Corresponding author.
E-mail address: siddhartha.roy@kit.edu (S. Roy).

2. Experimental procedure

2.1. Specimen material

The composite material was fabricated by the Materials Research Team of Aalen University of Applied Sciences, Germany, following a processing route thoroughly described in Ref. [19]. Commercially available alumina powder (CL2500 from Almatis GmbH, Germany with particle size 1.8 μm/d50 and nominal alumina content 99.8%) was used to prepare porous ceramic preforms. Cellulose fibres (Arbocel P290 from J. Rettenmaier and Söhne GmbH & Co. KG, Germany) having nominal average length of 150 μm were added as pore forming agent. The alumina powder particles were first deglomerated by wet ball milling, mixed with the pore forming agent and freeze-dried. The powders were subsequently pressed uni-directionally under 100 MPa applied pressure into plates having nominal dimensions $65 \times 45 \times 10\,\mathrm{mm}^3$ and then sintered in an electrically heated tube furnace under an oxidizing atmosphere. The sintering temperature was 1550 °C and during this process pyrolysis of the pore forming agents also occurred. Fig. 1 shows a scanning electron microscopy (SEM) micrograph of the uninfiltrated ceramic preform with a nominal ceramic content of 41 vol.%. Several regions with traces of cellulose fibres can be observed in this image (macroporosity), and one such location is indicated by an arrow. Micropores visible within the ceramic rich regions result from incomplete sintering of the preform. The porous preforms were subsequently infiltrated with a eutectic aluminium–silicon (AlSi12) melt via direct squeeze-casting along the same direction as that of powder pressing before sintering. Prior to squeeze-casting, the preform and the melt were preheated to 800 °C, while the tool was heated up to 420 °C. 100 MPa infiltration pressure was applied.

The metal/ceramic composite samples were fabricated in the form of plates. Five different plates with varying alumina contents were available. In the following, these plates are named as Types A–E. For ultrasonic analysis, several rectangular parallelepiped samples were cut from each plate using a 500 μm diameter diamond coated steel wire saw. The samples had nominal dimensions in the range of 6–10 mm and the numbers of samples in each composite type are listed in Table 1. For each sample, the direction parallel to the direction of preform pressing and squeeze-casting was marked as direction 1, and the two directions orthogonal to it were marked as directions 2 and 3, respectively. Density of each sample was determined following Archimedes' principle by immersing it in distilled water. Alumina content of each sample was determined from the measured density and assuming absence of any porosity. To calculate the alumina volume fraction, the density of alumina was taken as $3.90\,\mathrm{Mg\,m^{-3}}$ [20], while the density of AlSi12 was determined in the current study to be $2.66\,\mathrm{Mg\,m^{-3}}$. The average density and the alumina volume fraction of each composite type, along with their standard deviations are given in Table 1.

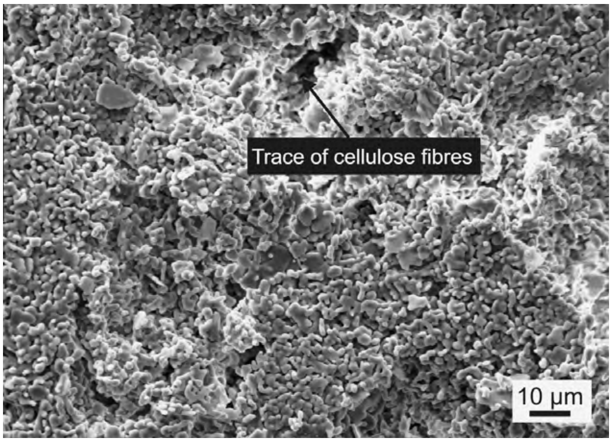

Fig. 1. SEM image of the ceramic preform with nominal ceramic content of 41 vol.%. The micrograph shows the face perpendicular to the direction of preform pressing and squeeze-casting. Trace of a cellulose fibre is shown by the arrow.

2.2. Ultrasonic analysis

Ultrasonic phase spectroscopy (UPS) was used to determine the longitudinal and the shear wave velocities along all three directions in each sample. Only a brief overview of the method is given here and for thorough description we refer to Ref. [17]. In this technique continuous, sinusoidal, elastic waves are used for the measurements and the phase shift occurring as the wave passes through the specimen is recorded as a function of frequency. The measurements were accomplished using an electronic network analyser (Advantest, model R3754A) and two identical broadband ultrasonic longitudinal wave (Panametrics, model V122 with nominal central frequency 7.5 MHz and diameter 9.5 mm) and shear wave (Panametrics, model V155 with nominal central frequency 5 MHz and diameter 12.7 mm) transducers. These transducers were attached to the opposite sides of the rectangular parallelepiped samples with the help of a water soluble couplant. The phase and the amplitude spectra were recorded in the frequency range from 10 kHz to 15 MHz for longitudinal wave measurements and in the range from 10 kHz to 10 MHz for shear wave measurements, respectively. In a non-dispersive medium, the velocity of the propagating wave can be determined following the relation:

$$V = -2\pi L/m \tag{1}$$

where L is the sample length along the propagating direction and m is the slope of the straight line fitted to the phase-frequency spectrum. Once the wave velocity is measured, the respective elastic constants can be determined using the relation:

$$C = \rho V^2 \tag{2}$$

where ρ is the sample density. In case of the measurements with longitudinal waves, the direction of vibration of the particles of the medium is parallel to the direction of wave motion. Hence, for each longitudinal elastic constant C_{ii} (i = 1–3), only the wave velocity along the direction of wave propagation V_i needs to be measured. For shear waves, the direction of vibration of the particles of the medium is orthogonal to the direction of wave motion. Following Rose [21], each shear elastic constant C_{ii} (i = 4–6) can be determined by either of the two wave velocities V_{xy} (where the first suffix is the direction of wave motion and the second suffix is the direction of particle motion). The velocities corresponding to C_{44}, C_{55} and C_{66} are V_{23} and V_{32}, V_{13} and V_{31}, and V_{12} and V_{21}, respectively. Therefore, nine different wave velocities (three longitudinal-wave velocities along three principal directions and two shear wave velocities for each of the three shear elastic constants) were measured for each sample.

To determine the three non-diagonal components of the stiffness matrix (C_{12}, C_{13}, C_{23}), 45° cuts were made at the opposite corners along the edges of one sample of Type A. Detail description of the sample geometry and the necessary methodology to determine these three constants are described in Ref. [22].

3. Results

Fig. 2 shows the optical micrographs of the composite material with alumina content of approximately 35 vol.%. Micrographs 'a' and 'b' correspond to the faces parallel to the direction of preform pressing and squeeze-casting. Micrograph 'c' shows the structure

Table 1
Densities, ceramic contents and longitudinal and shear wave velocities of each composite type. Values for each type are averaged over the number of samples in each type mentioned in the table.

Type	Density (Mg m^{-3})	Sample no.	Ceramic content (vol. fr.)	V_{11} (m s^{-1})	V_{22} (m s^{-1})	V_{33} (m s^{-1})	V_{23} (m s^{-1})	V_{32} (m s^{-1})	V_{13} (m s^{-1})	V_{31} (m s^{-1})	V_{12} (m s^{-1})	V_{21} (m s^{-1})
A	3.10 ± 0.06	20	0.35 ± 0.05	7583 ± 208	7789 ± 294	7776 ± 263	4106 ± 327	4079 ± 293	4094 ± 143	4146 ± 222	4006 ± 175	4060 ± 242
B	3.22 ± 0.06	13	0.45 ± 0.05	8006 ± 126	8186 ± 113	8239 ± 85	4483 ± 166	4467 ± 153	4375 ± 197	4417 ± 176	4342 ± 195	4421 ± 188
C	3.28 ± 0.09	13	0.50 ± 0.08	8199 ± 125	8537 ± 190	8507 ± 133	4732 ± 308	4645 ± 348	4548 ± 81	4669 ± 107	4408 ± 230	4627 ± 287
D	3.31 ± 0.06	20	0.53 ± 0.05	8332 ± 121	8513 ± 81	8583 ± 137	4588 ± 244	4593 ± 197	4575 ± 276	4589 ± 298	4589 ± 112	4629 ± 189
E	3.39 ± 0.07	20	0.59 ± 0.06	8692 ± 190	8956 ± 183	9008 ± 162	5040 ± 247	4946 ± 228	4790 ± 275	4866 ± 320	4901 ± 147	4960 ± 144

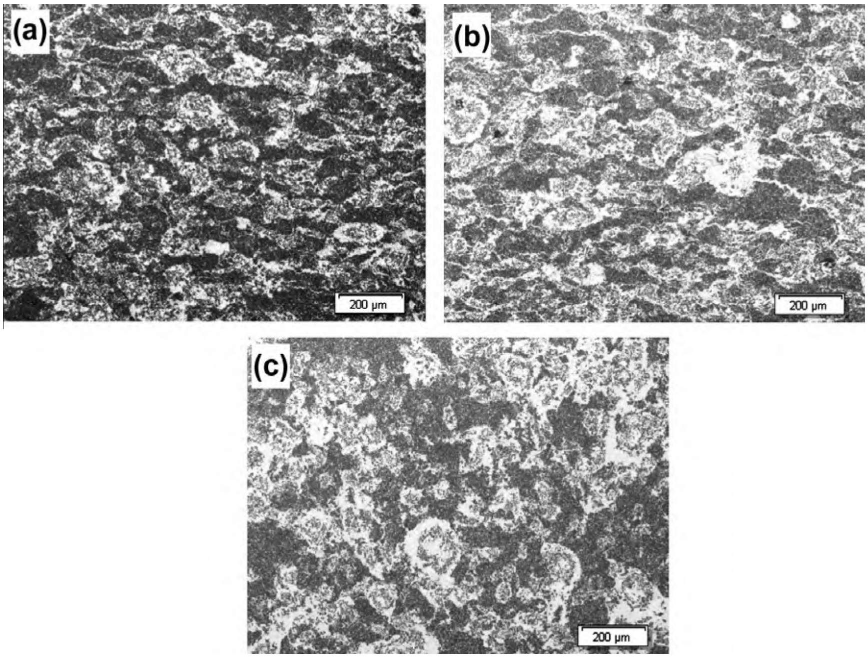

Fig. 2. Optical micrographs of the composite with alumina volume fraction $V_f = 0.35$. Micrographs (a and b) show the structure of the faces parallel to the direction of preform pressing and squeeze-casting, which are oriented along vertical direction in the images shown. Micrograph (c) shows the structure of the face perpendicular to the direction of squeeze-casting and preform pressing.

of the face perpendicular to the direction of preform pressing and squeeze-casting. All three images were taken from the same sample. In images ‘a’ and ‘b’, the direction of preform pressing and squeeze-casting is oriented along the vertical direction. Texture caused by preform pressing is clearly visible in the shown images. Distribution of the phases in micrograph ‘c’ is mostly random, while the phases are mostly aligned along the direction transverse to the press direction in micrographs ‘a’ and ‘b’. In these optical micrographs the darker phase is alumina while the brighter phase is AlSi12 alloy. The optical micrograph shows clusters rich with alumina while the regions away from the clusters are rich with the matrix alloy AlSi12. Fig. 3 shows a SEM image of the composite material. In this image the regions marked as AlSi12 are the locations of the original cellulose fibres shown in Fig. 1. Regions of metallic alloy visible within the alumina rich regions are the locations of the micropores within the sintered preform. Both these original micropores in the ceramic walls and the traces of the cellulose fibres between the ceramic walls are filled by the liquid metal during infiltration and give rise to the interpenetrating structure of the composite. Small amount of residual porosity remains in the MMC after infiltration.

Fig. 4 shows typical phase-frequency spectra obtained from UPS using longitudinal and shear wave transducers. In the current study it was observed that in almost all samples, the phase spectra obtained with both longitudinal and shear transducers were mostly linear with a constant slope over a significant range of frequency. This indicates that the measured wave velocities were independent of frequency (absence of dispersion). The spectra shown in Fig. 4 were obtained for wave propagation in the same

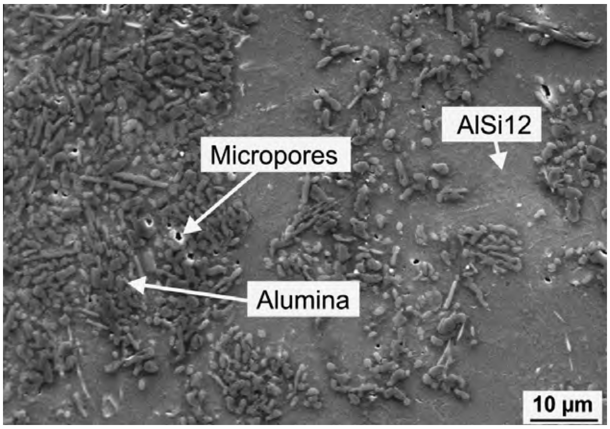

Fig. 3. SEM image of the composite material.

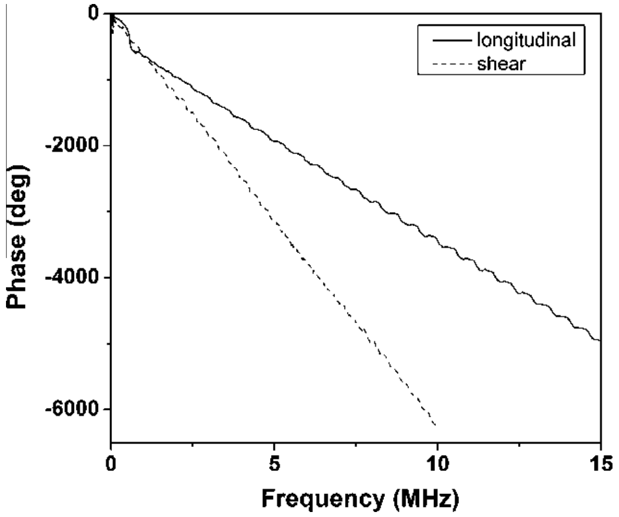

Fig. 4. Typical phase–frequency spectra obtained from ultrasonic analysis using longitudinal and shear wave transducers.

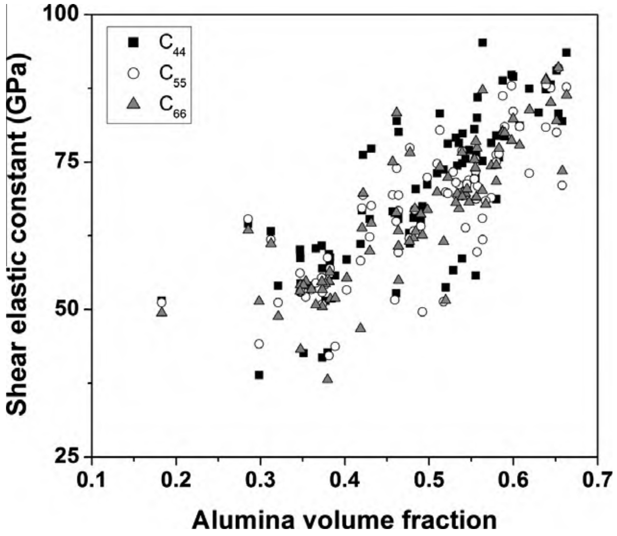

Fig. 6. Plot showing the variation of the shear elastic constants with ceramic content.

sample along the same direction. Following Eq. (1), as the shear wave propagation velocity in the material is significantly less than the longitudinal wave propagation velocity, the slope of the shear wave spectrum in Fig. 4 is significantly higher.

In Table 1 the measured longitudinal and shear wave velocities, averaged over all the samples within a composite type are listed. For each sample, the three longitudinal and the three shear elastic constants were determined following Eq. (2). Two shear wave velocities were determined for each shear elastic constant and the average of these two velocities was then used to determine the actual shear elastic constant. In almost all samples and for each shear elastic constant, the two shear wave velocities were almost equal within experimental uncertainties, suggesting that the composite had orthotropic or higher symmetry [21]. Figs. 5 and 6 show the variation of the longitudinal and the shear elastic constants with ceramic content in all composite samples. In spite of the considerable scatter, these plots show that in general the elastic constants increase with increasing ceramic content. The scatter in experimental data points may arise due to structural heterogeneities and defects such as residual porosity, imperfect bonding between the phases, particle agglomeration, and varying degrees of ceramic wall interconnections. The scatter in the data points for shear elastic constants is more than the data points for longitudinal elastic constants. This may be attributed to the enhanced experimental difficulty associated with shear wave measurements due to the additional constraint of aligning the sample properly along the direction of vibration of the particles of the medium. In individual samples, C_{11} was found to be marginally less than C_{22} and C_{33}, which themselves were almost equal to each other. The values of the average longitudinal-wave velocities in each composite type listed in Table 1 clearly show this. No such trend was observed in case of shear elastic constants, and Table 1 shows that the three average shear elastic constants in each composite type were equal to each other within experimental uncertainties.

Figs. 7 and 8 show the correlation of the experimentally determined average elastic constants in each composite type with the theoretical micromechanical models. As C_{22} and C_{33} were almost equal, their average is plotted in Fig. 7. Average of the three shear elastic constants in each composite type is plotted in Fig. 8. Error

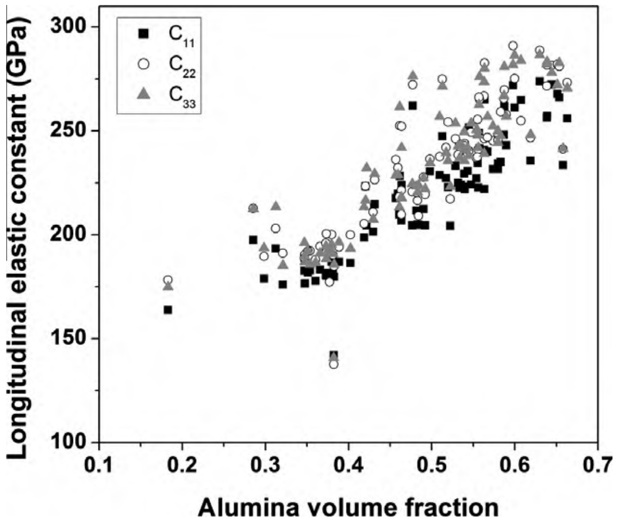

Fig. 5. Plot showing the variation of the longitudinal elastic constants with ceramic content.

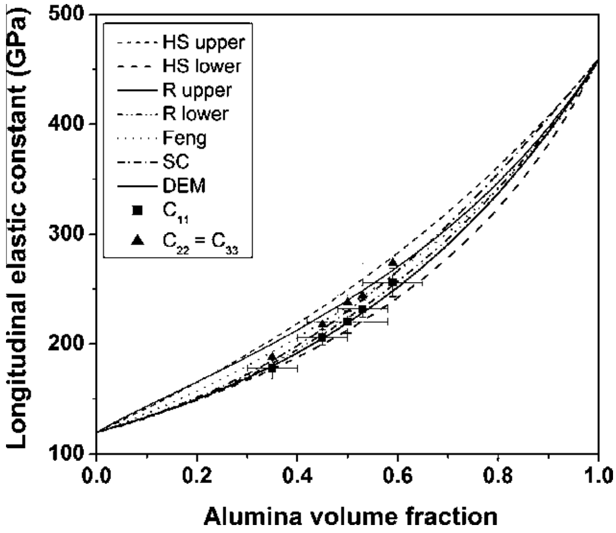

Fig. 7. Plot showing the correlation between the experimentally determined average longitudinal elastic constant of each composite type with theoretical models. Average of C_{22} and C_{33} is plotted.

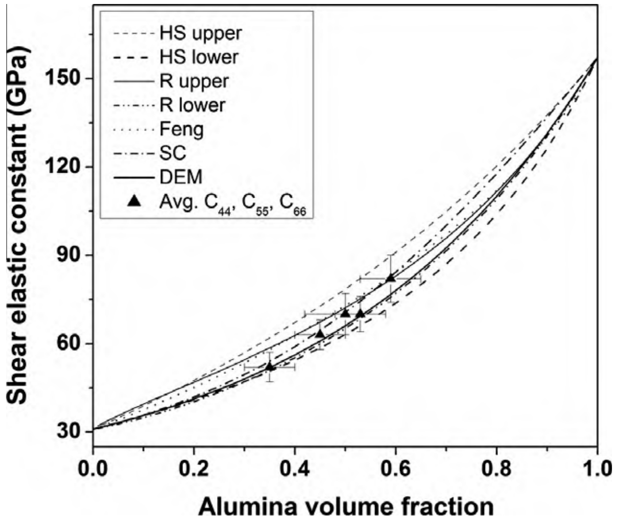

Fig. 8. Plot showing the correlation between the experimentally determined average shear elastic constant of each composite type with theoretical models. Experimental values show the average between C_{44}, C_{55} and C_{66}.

Table 2
Complete stiffness matrix of one sample of Composite Type A.

C_{11} (GPa)	C_{22} (GPa)	C_{33} (GPa)	C_{44} (GPa)	C_{55} (GPa)	C_{66} (GPa)	C_{23} (GPa)	C_{13} (GPa)	C_{12} (GPa)
176	190	189	62	54	49	61	67	68

bars in these plots correspond to standard deviation in volume fraction and the respective elastic constant within all samples of a particular composite type. Thorough description of the used micromechanical models is beyond the scope of this work and they can be found in the following Refs. ([14] for HS bounds, [15] for R bounds, [23] for F model, [24] for DEM model and [25] for SC model). Among the models, the HS bounds, the DEM and the SC models predict the bulk modulus and the shear modulus of a linear elastic isotropic spherical particle reinforced composite. The F model is developed for multiphase interpenetrating composites while the R-model considers isolated cubic inclusions in a continuous matrix. These two models give expressions for the Young's modulus and the shear modulus of the composite. Isotropy has been assumed to calculate the model predictions in the present work. The actual mathematical formulations for the model calculations can be found in Refs. [11,26]. To calculate the model predictions, the Young's modulus and the Poisson's ratio of alumina were taken as 390 GPa and 0.24, respectively [27]. The Young's modulus and the Poisson's ratio of AlSi12 were measured during the present study and they were 82 GPa and 0.326, respectively. Other elastic constants were determined from these values assuming isotropy. For isotropic behavior, the models predicted the technical constants of the composite (Young's modulus (E), bulk modulus (K), shear modulus (G) and Poisson's ratio (ν)). The expression for the shear modulus is identical to the expression for the shear elastic constant. The expression for the longitudinal elastic constant of the composite was determined using the relation:

$$C_{ii\ (i=1-3)} = \frac{(3K+2G)(6K+2G)}{6(3K+G)} \tag{3}$$

Nine elastic constants of one sample of Composite Type A were measured to determine the complete stiffness matrix assuming orthotropic symmetry. The results are shown in Table 2. The compliance matrix for this sample was subsequently determined by matrix inversion. The technical constants (Young's moduli, shear moduli and Poisson's ratios) were finally determined using the standard relation for orthotropic symmetry [22]. These technical constants are listed in Table 3.

4. Discussions

Ceramic content in each sample was determined assuming no porosity. However, Fig. 3 shows presence of small amount of residual porosity in the composite. As shown by Weidenmann et al. [28], presence of porosity may lead to a deviation in the calculated ceramic volume content. They attributed the residual porosity in the MMC to stronger shrinkage of the matrix than the ceramic particles during cooling from the solidification temperature and to incomplete infiltration due to insufficient infiltration pressure. As 100 MPa pressure was applied during squeeze-casting to fabricate the MMC in the present study, the second term in their calculation has been neglected here. Following the modified expression in Eq. (4) in Ref. [28], the amount of residual porosity in the studied MMC samples was estimated to lie in the range of 0.1–0.5 vol.%. This may shift the calculated alumina content in the composite samples to a value approximately 0.2–1.1 vol.% higher than under the assumption with no porosity.

Due to the random structure of the composite, the material is expected to behave isotropically. The observed marginally reduced stiffness along direction 1 may result from either powder pressing or squeeze-casting. UPS on uninfiltrated ceramic preforms showed that the longitudinal wave velocity along direction 1 was about 30–50% less than the longitudinal-wave velocities along directions 2 and 3, which were similar. Therefore, it can be concluded that powder pressing prior to sintering of the preform caused the observed marginal reduction in C_{11}. Table 1 however shows that in the composite the velocity V_1 is only 2–5% less than the velocities V_2 and V_3. This suggests that as a result of infiltration, the composite exhibits much less pronounced anisotropy in comparison to the uninfiltrated preform. The continuous compliant AlSi12 phase increases the stiffness of the porous preform along all directions; however, this increase is most pronounced along the most compliant direction of the preform.

Figs. 7 and 8 show that the measured average longitudinal and shear elastic constants lie within the HS upper and lower bounds. The predictions of R bounds lie within the HS bounds. The extent to which the individual theoretical models predict the experimentally determined elastic constant may be expressed as [11]:

$$\%D = \frac{C_{ii}^{model} - C_{ii}^{experimental}}{C_{ii}^{model}} \times 100\% \tag{4}$$

This quantity is listed in Table 4 for individual models. The table clearly shows that when all the elastic constants are considered, the predictions from the SC model are most accurate, the maximum deviation being approximately 6% for the shear elastic constant in Composite Type D. The predictions from DEM model lie between the predictions from SC model and HS lower. It predicts the composite behavior most accurately when the elastic constant C_{11} is considered. In case of shear elastic constants, the accuracy of the DEM model is close to the SC model, however, it is rather inaccurate when elastic constants C_{22} and C_{33} are considered. Although F model is specially designed for interpenetrating composites, the table shows that apart from the elastic constants C_{22} and C_{33}, its accuracy for the studied material is significantly less in comparison to SC and DEM models. Table 4 typically shows that with increasing alumina content, the $\%D$ progressively becomes less positive for HS upper and it becomes more negative for HS lower. This trend is similar for all elastic constants. It suggests that as the alumina content of the composite increases, the elastic constants of the composite are predicted more accurately by the HS upper bound

Table 3
Technical constants of one sample of Composite Type A.

E_1 (GPa)	E_2 (GPa)	E_3 (GPa)	G_{23} (GPa)	G_{13} (GPa)	G_{12} (GPa)	ν_{21}	ν_{31}	ν_{12}	ν_{32}	ν_{13}	ν_{23}
140	156	156	62	54	49	0.305	0.298	0.272	0.214	0.267	0.215

Table 4
Table showing the deviation between the experimentally determined elastic constants and model predictions.

Type	Expt.	HS_U	%D	HS_L	%D	R_U	%D	R_L	%D	F	%D	SC	%D	DEM	%D
C_{11}															
A	178 ± 10	204.5	12.9	177.1	−0.5	200.3	11.1	182.3	2.4	192.8	7.7	185.1	3.8	180.1	1.1
B	206 ± 7	233.7	11.9	199.9	−3.1	226.0	8.9	208.8	1.3	219.7	6.3	213.7	3.6	205.0	−0.5
C	220 ± 10	249.4	11.8	212.8	−3.4	239.9	8.3	223.7	1.6	234.4	6.1	230.0	4.3	219.3	−0.3
D	232 ± 8	259.1	10.5	221.1	−4.9	248.7	6.7	233.2	0.5	243.5	4.7	240.4	3.5	228.5	−1.5
E	256 ± 13	279.5	8.4	239.2	−7.0	267.3	4.2	253.5	−1.0	262.7	2.6	262.8	2.6	248.3	−3.1
Average of C_{22} and C_{33}															
A	188 ± 13	204.5	8.0	177.1	−6.1	200.3	6.2	182.3	−3.1	192.8	2.5	185.1	−1.6	180.1	−4.4
B	218 ± 7	233.7	6.9	199.9	−8.8	226.0	3.8	208.8	−4.2	219.7	1.0	213.7	−1.8	205.0	−6.1
C	238 ± 12	249.4	4.6	212.8	−11.9	239.9	0.8	223.7	−6.4	234.4	−1.5	230.0	−3.5	219.3	−8.5
D	244 ± 9	259.1	5.8	221.1	−10.4	248.7	1.9	233.2	−4.7	243.5	−0.2	240.4	−1.5	228.5	−6.8
E	274 ± 11	279.5	2.2	239.2	−14.3	267.3	−2.3	253.5	−7.9	262.7	−4.1	262.8	−4.1	248.3	−10.1
Average of C_{44}, C_{55} and C_{66}															
A	53 ± 5	62.0	15.0	50.6	−4.1	58.6	10.1	51.0	−3.4	58.0	9.2	54.0	2.5	51.9	−1.5
B	63 ± 5	72.8	13.4	58.6	−7.5	67.3	6.5	60.0	−5.0	67.7	6.9	64.6	2.4	60.9	−3.4
C	70 ± 7	78.6	11.3	63.2	−10.3	72.2	3.5	65.2	−6.9	72.9	4.4	70.6	1.3	66.1	−5.4
D	70 ± 6	82.2	14.4	66.2	−6.3	75.3	6.5	68.6	−2.6	76.2	7.7	74.5	5.6	69.4	−1.3
E	82 ± 8	89.7	8.3	72.7	−13.3	81.9	−0.6	75.9	−8.5	83.1	0.9	82.9	0.7	76.8	−7.3

Table 5
Table showing the accuracy of the measured technical constants.

E_1/ν_{12} (GPa)	E_2/ν_{21} (GPa)	E_1/ν_{13} (GPa)	E_3/ν_{31} (GPa)	E_2/ν_{23} (GPa)	E_3/ν_{32} (GPa)
514.71	511.47	524.34	523.49	725.58	728.97

than the HS lower bound. This can be explained by the fact that the HS-model considers an isolated spherical phase coated with a concentric matrix phase. Diameters of the spheres depend upon the volume fraction of the individual phases. As discussed by Torquato et al. [29], in case of the lower bound, the compliant matrix is the outer phase and the arrangement of the stiffer phase can be regarded to be most disconnected. In case of the upper bound, the compliant phase is the inner phase and the arrangement of the stiffer phase can be regarded to be most connected. In the interpenetrating composite under study, both phases are continuous, and hence the simplistic HS-model is not ideally suited to predict the elastic behavior of such composites. In spite of this limitation, comparison of the experimental results of the current study with theoretical HS bounds provides valuable insight because of two reasons. Firstly, in a previous study, Young's modulus of an interpenetrating MMC over a range of ceramic content was found to lie close to the HS lower bound [30]. Secondly, the HS bounds are much more rigorous than the simple rule of mixtures models, which are considered to be strict upper and lower bounds. However, the proximity of the experimentally determined elastic constants at high ceramic content to the HS upper bound contradicts the results obtained by Moon et al. [11]. For Al–Al_2O_3 interpenetrating composites they found that even at ceramic content in the range of 73–97 vol.% the Young's modulus was closer to the HS lower bound.

Table 2 and 3 shows that although nine elastic constants of one sample were determined assuming orthotropic symmetry of the composite, the elastic constants were similar along directions 2 and 3. Hence, the composite behaves more like a material with transverse isotropic symmetry with respect to direction 1. Determination of the complete stiffness matrix also allows predicting the off-axis behavior of the material. Following Jones [31], the Young's moduli and Poisson's ratios of an orthotropic material must satisfy the following relations:

$$\frac{E_i}{\nu_{ij}} = \frac{E_j}{\nu_{ji}} \quad i,j = 1,2,3 \tag{5}$$

and

$$\Delta = 1 - \nu_{12}\nu_{21} - \nu_{23}\nu_{32} - \nu_{31}\nu_{13} - 2\nu_{21}\nu_{32}\nu_{13} > 0 \tag{6}$$

In the present study Δ was equal to 0.757, while Table 5 shows that Eq. (5) is also valid within slight uncertainties. These suggest that the technical constants determined in the current study are accurate and theoretically valid.

5. Conclusions

In depth elastic analysis of an interpenetrating AlSi12–Al_2O_3 composite was carried out in this study using ultrasound phase spectroscopy. Following conclusions can be drawn:

- Preform pressing prior to sintering marginally reduces the longitudinal elastic constant of the composite along the press direction. The composite behaves like a transverse isotropic material with respect to this direction. The compliant metallic alloy functions as a stiff backbone to stiffen the composite along the press direction in comparison to uninfiltrated preform.
- Results show that the experimentally determined longitudinal and shear elastic constants lie within the Hashin–Shtrikman bounds. At low ceramic contents the values are closer to the Hashin–Shtrikman lower bound, while at high ceramic content the Hashin–Shtrikman upper bound is more accurate.

- Among the micromechanical models considered, self consistent model predicted the average elastic constants of the composite over the complete ceramic vol.% range most accurately.
- Complete stiffness matrix of one sample was determined and the technical constants were determined there from.

References

[1] Chawla N, Chawla KK. Metal matrix composites. New York (USA): Springer Science + Business Media, Inc.; 2006.

[2] Prielipp H, Knechtel M, Clausen N, Streiffer SK, Müllejans H, Rühle M, et al. Strength and fracture toughness of aluminum/alumina composites with interpenetrating networks. Mater Sci Eng A 1995;197:19–30.

[3] Sternitzke M, Knechtel M, Hoffmann M, Broszeit E, Rödel J. Wear properties of alumina/aluminum composites with interpenetrating networks. J Am Ceram Soc 1996;79:121–8.

[4] Feng HJ, Moore JJ. In situ combustion and ceramic-metal synthesis of dense ceramic interpenetrating phase composites. Met Mater Trans 1995;26B:265–73.

[5] Liu W, Köster U. Microstructures and properties of interpenetrating alumina/aluminium composites made by reaction of SiO_2 glass preforms with molten aluminium. Mater Sci Eng A 1996;A210:1–7.

[6] Horvitz D, Gotman I, Gutmanas EY, Clausen N. In situ processing of dense Al_2O_3–Ti aluminide interpenetrating phase composites. J Eur Ceram Soc 2002;22:947–54.

[7] Xie X-Q, Zhang D, Fan T-x, Sakata T, Mori H, Okabe T, et al. The fabrication of composites with interpenetrating networks based on wood ceramics. Mater Lett 2002;56:102–7.

[8] San Marchi C, Kouzeli M, Rao R, Lewis JA, Dunand DC. Alumina–aluminum interpenetrating-phase composites with three-dimensional periodic architecture. Scripta Mater 2003;49:861–6.

[9] Waschkies T, Oberacker R, Hoffmann MJ. Control of lamellae spacing during freeze-casting of ceramics using double-side cooling as a novel processing route. J Am Ceram Soc 2009;92:S79–84.

[10] Roy S, Butz B, Wanner A. Damage evolution and domain-level anisotropy in metal/ceramic composites exhibiting lamellar microstructures. Acta Mater 2010;58:2300–12.

[11] Moon RJ, Tilbrook M, Hoffman M, Neubrand A. Al–Al_2O_3 composites with interpenetrating network structures: composite modulus estimation. J Am Ceram Soc 2005;88:666–74.

[12] Peng HX, Fan Z, Evans JRG. Bi-continuous metal matrix composites. Mater Sci Eng A 2001;303:37–45.

[13] Tilbrook MT, Moon RJ, Hoffman M. On the mechanical properties of alumina–epoxy composites with an interpenetrating network structure. Mater Sci Eng A 2005;A393:170–8.

[14] Hashin Z, Shtrikman S. A variational approach to the theory of the elastic behavior of multiphase materials. J Mech Phys Solids 1963;11:127–40.

[15] Ravichandran KS. Elastic properties of two phase composites. J Am Ceram Soc 1994;77:1178–84.

[16] Tuchinskii LI. Elastic constants of pseudoalloys with a skeletal structure. Poroshk Metall 1983;7:85.

[17] Wanner A. Elastic moduli measurements of extremely porous ceramic materials by ultrasonic phase spectroscopy. Mater Sci Eng A 1998;A248:35–43.

[18] Roy S, Gibmeier J, Kostov V, Weidenmann KA, Nagel A, Wanner A. Internal load transfer in a metal matrix composite having a three dimensional interpenetrating structure. Acta Mater 2011;59:1424–35.

[19] Huchler B, Staudenecker D, Weidler T, Mattern A, Nagel A, Kallien L, Hoffmann, M. Einfluss von Porenstruktur und Chemie auf die Herstellung von Partkelverstärkten Preform – MMCs im Squeeze-Casting und Druckgussverfahren. In: Proceedings of Symposium Verbundwerkstoffe und Werkstoffverbunde, Frankfurt, Germany; 2005.

[20] Engineered Materials Handbook, vol 1. Composites. ASM International; 1987.

[21] Rose JL. Ultrasonic waves in solid media. Cambridge (UK): Cambridge University Press; 1999.

[22] Van Buskirk WC, Cowin SC, Ward RN. Ultrasonic measurement of orthotropic elastic constants of bovine femoral bone. J Biomech Eng 1981;103:67–72.

[23] Feng XQ, Tian Z, Liu YH, Yu SW. Effective elastic and plastic properties of interpenetrating multiphase composites. Appl Compos Mater 2004;11:33–55.

[24] Torquato S. Random heterogeneous materials. New York (USA): Springer Verlag; 2002.

[25] Hill R. A self-consistent mechanics for composite materials. J Mech Phys Solids 1965;13:213–22.

[26] Mueller R, Mortensen A. Simplified prediction of the monolithic uniaxial stress-strain curve of non-linear particulate composites. Acta Mater 2006;54:2145–55.

[27] Shackelford JF, Alexander W. Materials science and engineering handbook. CRC Press; 2001.

[28] Weidenmann KA, Tavangar R, Weber L. Rigidity of diamond reinforced metals featuring high particle contents. Compos Sci Technol 2009;69:1660–6.

[29] Torquato S, Yeong CLY, Rintoul MD, Milius DL, Aksay IA. Elastic properties and structure of interpenetrating boron carbide/aluminum multiphase composites. J Am Ceram Soc 1999;82:1263–8.

[30] Daehn GS, Starck B, Xu L, Elfishawy KF, Ringnalda J, Fraser HL. Elastic and plastic behavior of a co-continuous alumina/aluminum composite. Acta Mater 1996;44:249–61.

[31] Jones RM. Mechanics of composite materials. USA: Taylor & Francis; 1999.